Available online at www.sciencedirect.com
ScienceDirect
Ceramics International 35 (2009) 3185–3194
CERAMICS INTERNATIONAL
www.elsevier.com/locate/ceramint

Evaluation of sintering stresses of an Al_2O_3 powder with a self-loading apparatus

Takayasu Ikegami [a,*], Nobuo Iyi [b], Isao Sakaguchi [c]

[a] *Strategy Office, National Institute for Materials Science, 1-2-2 Sengen, Tsukuba-shi, Ibaraki 305-0047, Japan*
[b] *Nanoscale Materials Center, National Institute for Materials Science, 1-1 Namiki, Tsukuba-shi, Ibaraki 305-0047, Japan*
[c] *Optronic Materials Center, National Institute for Materials Science, 1-1 Namiki, Tsukuba-shi, Ibaraki 305-0047, Japan*

Received 26 March 2009; received in revised form 3 April 2009; accepted 12 May 2009
Available online 6 June 2009

Abstract

The sintering stress of an Al_2O_3 powder, σ_s, is evaluated from an equation $\sigma_s = F_s/\rho S_a$, where F_s is the uniaxial tensile force necessary to just stop the sintering contraction, ρ is the relative density, and S_a is the cross-sectional area. During densification, σ_s increases to the maximum at a relative density of 85%, and then abruptly decreases. The variation of σ_s in the intermediate sintering stage suggests a simple cubic packing of particles. Densification in the final sintering stage is explained by shrinkage of the pores at the corners where four tetrakaidecahedra meet. The present surface tensions of the Al_2O_3 powder evaluated from the σ_s roughly equal a reported value.

Keywords: A. Sintering; B. Surface; C. Mechanical properties; D. Strength; F. Al_2O_3

1. Introduction

Sintering is a key process controlling properties of ceramics and powder metallurgy [1]. A lot of recent studies have focused on numerical simulation to describe microstructural evolution during sintering [2–5]. The validity of the simulated results however depends on both the adequateness of the sintering model and the quality of the initial conditions. Not only theoretical study but also experimental one is still necessary.

Fundamental equations on sintering kinetics [6–9] have been derived based on simple models such as the contact of two particles [6,7] and cylindrical pores along grain edges [9]. A majority of the derived equations [6–8] consists of a few constants and four explicit parameters defining sintering rate. The latter are surface tension, particle size, diffusion coefficient and temperature. The measurements of sintering temperature and particle size are easy. Various kinds of diffusion coefficients have been measured [10,11], and many additives were examined to improve sinterability of ceramic powders by increasing atomic mobility [12–14].

The surface tension is the driving force for sintering [6–9], and not a few studies have been devoted to describing the microstructure of sintered compacts using both appropriate values of the surface and the interfacial tensions [2–5,15,16]. In contrast, few empirical studies have tried to measure the driving force for sintering. This may be attributed to the difficulty in measurement of the surface tension or the sintering force.

The so-called ‘‘zero-creep’’ method is useful to measure the surface tensions of metals [17], and those of crystals were also evaluated from the forces necessary for the propagation of cleavage cracks [18]. If one finds a solvent into which the solubility of a powder is large enough to measure the heat of solution, the surface enthalpy of the solid concerned also can be determined calorimetrically [19]. Such solvents have been rarely found for ceramic or metallic powders.

Dawihl and Rix [20], and Gregg and Rhines [21] evaluated the sintering forces of Cu from the uniaxial tensile forces necessary to just stop the sintering contraction. This method is similar to the zero-creep method, which was also applied to measurement of the sintering pressure of TiO_2 by Cheng and Raj [22]. Rahaman et al. evaluated the sintering stresses of a CdO powder using a loading dilatometer [23]. The apparatuses

* Corresponding author at: Strategy, National Institute for Materials Science, 1-2-2 Sengen, Tsukuba-shi, Ibaraki 305-0047, Japan.
Tel.: +81 29 859 2000x6827; fax: +81 029 859 2025.
E-mail address: Ikegami.Takayasu@nims.go.jp (T. Ikegami).

0272-8842/$36.00
doi:10.1016/j.ceramint.2009.05.004

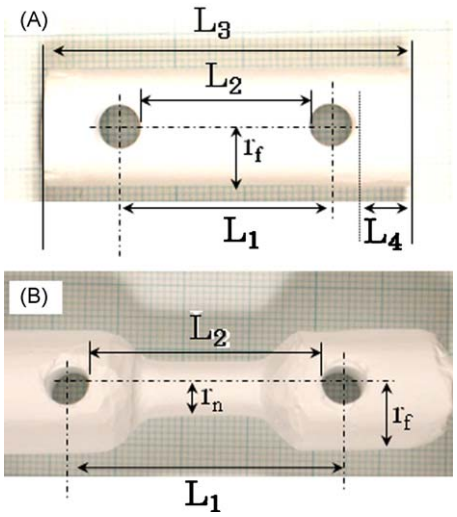

Fig. 1. Two typical specimens for measurement of sintering force.

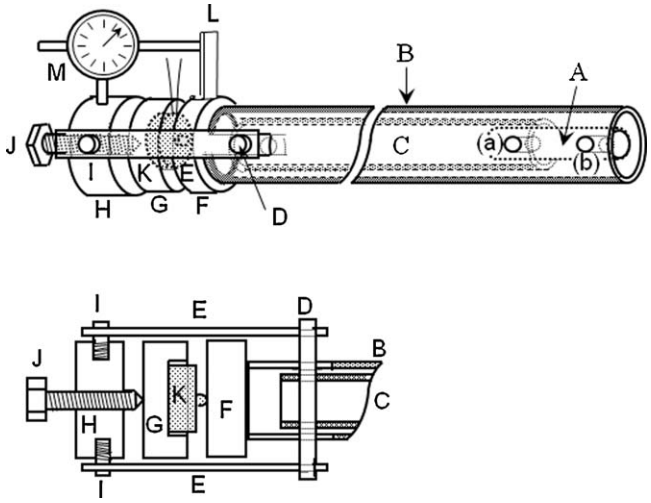

Fig. 2. A schematic self-loading apparatus: specimen A; Alumina tube B; Alumina tube C; Rod D connecting Alumina tube C and Timbers E; Disks F, G and H; Hook I; Bolt J; a load cell K; Stopper L; a dial gauge M; (a) and (b) bores with a diameter of 5 mm.

used in the reported methods require delicate operations [21–24]. Since the present apparatus automatically inhibits the axial shrinkage of a specimen, the sintering force was measured without controlling the shrinkage concerned.

2. Experimental procedures

A commercially available Al_2O_3 powder (TM-DAR, Taimei Chem. Co. Ltd., Nagano, Japan, with impurities of Si = 11–15 ppm, Fe = 9–10 ppm, Na = 3–4 ppm, K = 1–4 ppm, Ca = 1–2 ppm and Mg = 1 ppm) was examined. The specific surface area of the as-received powder, S_p, was measured by the BET method with N_2 gas at −196 °C using an automatic surface area analyzer (Model 4201, Beta Scientific Co., Long Island, N.Y.).

The powder was hydrostatically pressed at 200 MPa in rubber bags. The resultant powder compacts were cylinders with a diameter of 15–20 mm and a length of 150 mm. They were calcined at 900 °C for 2 h in flowing oxygen gas, and thereby the machinable specimens were obtained. Most the calcined powder compacts were shaped into simple rods, Type A, with a suitable radius on a lathe. Dumbbell rods, Type B, were made by scraping the rest calcined powder compacts with a knife. A bore of 6 mm diameter was made at 10 mm from each end of these specimens on a drill press. The distance between the bores was 30 mm for most specimens. Fig. 1 shows typical examples of them, in which r_f is the full radius of Type A or Type B, r_n is the neck radius of Type B, L_1 is the length between the centers of the bores, L_2 is the length of the mass between the bores, L_3 is the sample length and L_4 is the length of the part which was free from the tension caused by the sintering force. Some specimens were pre-fired to various temperatures in a range between 1160 and 1360 °C at a heating rate of 1.25 °C/min, and then cooled down to room temperature.

Fig. 2 shows a schematic loading apparatus. Two silicon carbide, SiC, rods of 5 mm diameter in bores (a) and (b) connected each end of specimen A and the end of Alumina tubes B and C, with the bore respectively. The other end of Alumina tube B was placed on Disk F, and that of Alumina tube C was connected to Disk H via Rod D, Timber E and Hook I. A compression load cell K was set on Disk G. Stopper L was fastened on Disk F. Shrinkage of the specimen resulted in pulling Disk H, which pushed the compression load cell K via Bolt J and Disk G. Bolt J is equipped to adjust the clearances between various parts such as the specimen, Alumina tube B, Alumina tube C, the load cell, Disk F, Disk G and Disk H. A dial gauge M was used to monitor shrinkage of the specimen during firing. The parts of the loading apparatus, except the alumina tubes and the SiC rods, were made of steel.

The loading apparatus with a specimen was set in a SiC furnace with a diameter of 400 mm and length of 600 mm. The specimen was heated at a rate of 10 °C/min to 900 °C, from which the heating rate was changed to 1.25 °C/min. In the case of an unfired specimen, this heating was continued. When the load cell indicated a decrease of the apparent sintering force, the loading apparatus was pulled by about 150 mm from the furnace to stop densification of the specimen, and the electric power of the furnace was turned off. If the specimen was a pre-fired one, Bolt J was rotated at a scheduled point, the pre-firing temperature minus 40 °C, to apply a stress of about 0.5–1 MPa to the specimen. Further operation was done by the same method as that for the unfired specimen.

The apparent sintering stress, σ_{sa}, was calculated from Eq. (1) [21].

$$\sigma_{sa} = F_L/\pi r_c^2 \rho \quad (1)$$

where F_L is the load to the load cell, ρ is the relative density, and r_c is the cross-sectional radius of the specimen. After measurement of F_L, the specimen was cut into several parts, of which the densities were measured by the Archimedes method in water as an immersion medium.

Pellets with a diameter of 6 mm and a thickness of 6 mm were fabricated by cold isostatic pressing at 200 MPa. The relative density of a green compact, ρ_o, was calculated from its

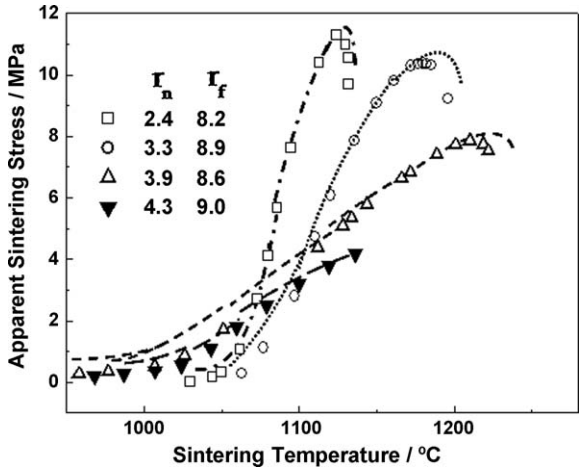

Fig. 3. Apparent sintering stresses, σ_{sa}, of type B calculated with the neck radii, r_n.

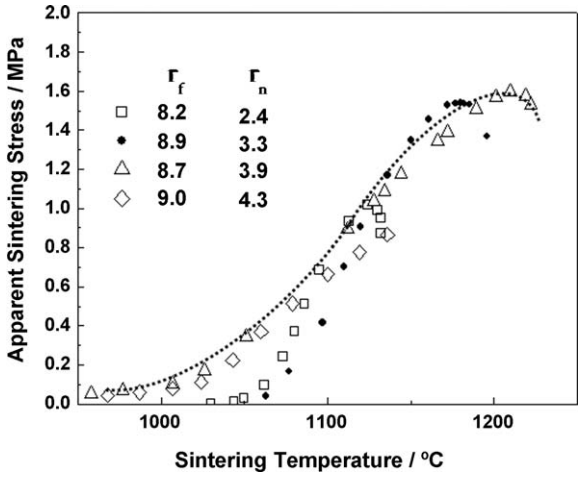

Fig. 4. Apparent sintering stresses, σ_{sa}, of type B calculated with the full radii, r_f.

dimensions, weight and theoretical density, ρ_t. Constant-rate-of-heating (CRH) sintering was performed using a thermo-mechanical analyzer (Model TMA 1700, Rigaku). The relative density of a sintered compact, ρ, was calculated from Eq. (2) using ρ_o and TMA linear shrinkage data, $\Delta L/L_o$:

$$\rho = \rho_o/(1 - \Delta L/L_o)^3 \quad (2)$$

where L_o is the initial sample length and $\Delta L = L_o - L$, where L is the instantaneous sample length.

3. Results

The S_p and the ρ_o of the present powder were 15.4 m^2/g and 56.5%, respectively. The particle radius of the powder, r_o, was estimated by $3/\rho_t S_p$. According to a previous paper [25], the average radius of grains in a sintered specimen, r, was given by

$$r = r_o[0.537 + 20.7/(100 - \rho) - 19.0/(100 - \rho)^2] \quad (3)$$

Fig. 3 shows apparent sintering stress, σ_{sa}, of Type B calculated from Eq. (1) with r_n as r_c. As can be seen there, σ_{sa} markedly increased with a decrease in r_n. When r_f is used as r_c, the variations of σ_{sa} in Fig. 4 were described by a single curve. The open and the shaded symbols in Fig. 5 show the σ_{sa}s of Type A, which were independent of r_f and L_1.

After F_L measurement, the values of L_1, L_2, L_3 and r_f of an unfired specimen decreased by 2.5%, 7%, 8% and 10%, respectively. In the case of a pre-fired specimen, L_1 decreased negligibly irrespective of pre-firing temperature. In contrast, the values of L_2, L_3 and r_f appreciably decreased by 8.0%, 2.7% and 8.0% for pre-firing to 1200 °C, 6%, 3% and 4.5% for pre-firing to 1240 °C, and 2.8%, 1.1% and 2.7% for pre-firing to 1280 °C, respectively.

Fig. 6 shows relative densities before and after sintering force measurement as a function of pre-firing temperature: (●) before the measurement, (□) the part, ρ_s, where the tension caused by the sintering force was applied, and (△) a part, ρ_f, free from the tension. Since all the specimens were calcined at

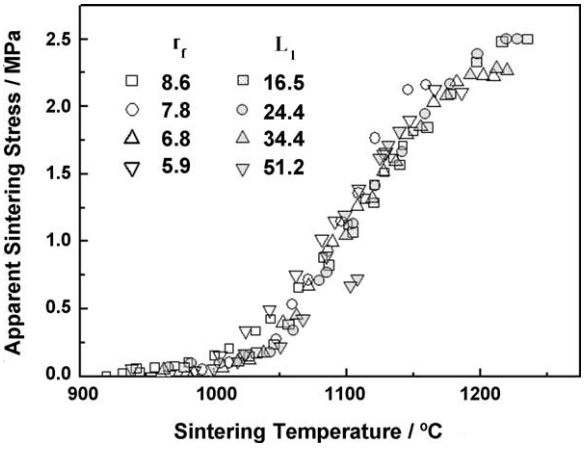

Fig. 5. The apparent sintering stresses, σ_{sa}, of type A.

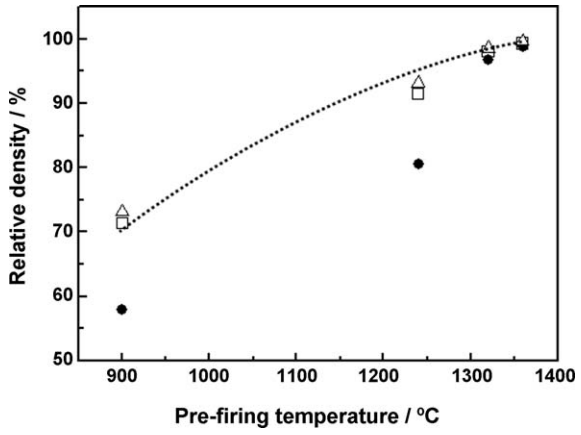

Fig. 6. Relative densities before and after sintering force measurement as a function of pre-firing temperature: (●) before the F_L measurement, (□) the parts where the tension caused by the sintering force was applied, ρ_s, (△) parts free from the tension, ρ_f. Since all the specimens were calcined at 900 °C to make them machinable, the data of the unfired specimen are plotted at 900 °C.

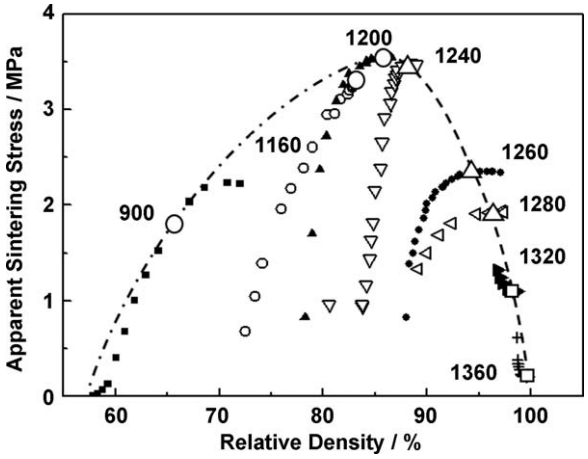

Fig. 7. Relationships between apparent sintering stresses, σ_{sa}, and relative density, ρ. (○) The contacts of point between the chain line and σ_{sa} curves, and (△ and □) the inflection points of σ_{sa} curves.

900 °C to make them machinable, the densities of an unfired specimen are plotted at the temperature of 900 °C in Fig. 6. As can be seen there, a considerable difference (about 2–3%) between ρ_f and ρ_s is noticed for the unfired specimen. This difference, however, became negligible with an increase in pre-firing temperature.

Fig. 7 shows relationships between σ_{sa} and ρ. The chain curve shows the envelope of the σ_{sa} curves of the specimens both unfired and pre-fired to 1160–1200 °C. The broken curve is the locus describing the inflection points of the σ_{sa} curves of the specimens pre-fired to 1240–1360 °C.

4. Discussion

4.1. Role of small clearances between various parts in the loading apparatus

Although being calcined at 900 °C, the specimens were still brittle. When a small tension was applied to calcined specimens for complete elimination of the clearances mentioned above, some of them were broken during F_L measurement. Even if a specimen did not break, the measured F_L was considerably small. These results suggested that the tension caused by the sintering force with the cooperation of the externally applied tension broke a considerable amount of contacts between particles in the specimen [26]. In order to avoid the break of contacts between particles, small clearances were put between various parts in the initial arrangement of the loading apparatus. While the clearances mentioned above disappeared by heating, both neck growth and small shrinkage between particles occurred, and the proper sintering force was able to be measured.

4.2. Two-dimensional and three-dimensional shrinkages

Since the present apparatus inhibited the axial shrinkage of a specimen, the two-dimensional shrinkage perpendicular to the axial direction was expected. The sum of cross-sectional areas of diffusion paths per unit cube is estimated to be proportional to the number of dimensions. The two-dimensional mass transfer per unit cube and per unit time equals two thirds of the three-dimensional mass transfer per unit cube and per unit time. Eq. (4) is derived from a kinetic equation for CRH sintering [27] under the condition that relative density at T_2 for two-dimensional sintering equals that at T_3 for three-dimensional sintering.

$$\frac{2}{3}\exp\left[-\frac{Q}{R(T_2+273)}\right] = \exp\left[-\frac{Q}{R(T_3+273)}\right] \quad (4)$$

where Q is the activation energy for diffusion of the atoms, and R is the gas constant. The T_3 for a given T_2 is calculated from Eq. (4) with a reported Q (=610 kJ/mol) value [25]. The ρ_f and ρ_s of a specimen fired to T_2 were approximated by the relative densities calculated from the shrinkages by CRH sintering to T_2 and T_3, respectively. A difference between ρ_f and ρ_s is nearly zero% at $T_2 = 900$ °C, increases to the maximum of 2.2% at $T_2 = 1220$ °C, and then gradually decreases to 0.3% at $T_2 = 1400$ °C. These values are well consistent with the empirical data in Fig. 6. For example, the aforesaid maximum difference was close to the difference between ρ_f and ρ_s for the unfired specimen, which had been quenched from about 1240 °C because of decrease of F_L. This temperature nearly equaled 1220 °C. Furthermore, a difference between ρ_f and ρ_s in Fig. 6 decreased with an increase in quenching temperature.

4.3. Specimen geometry valid to evaluate sintering stress

Fig. 3 shows σ_{sa} increasing with a decrease in r_n. In contrast, σ_{sa}s in Figs. 4 and 5 are described by respective single curves, regardless of the values of r_f, r_n and L_1. From these data, r_f is valid to estimate the sintering stress independent of geometry of a specimen.

For Type B, the sintering force equaled $\pi {r_n}^2 \rho\sigma_s$ at the neck and $\pi {r_f}^2 \rho\sigma_s$ at a location with the full radius, where σ_s is the proper sintering stress dependent on the porosity of the sintered body. The tension produced by the latter force operated at every location in the mass L_2. The difference between these forces acts as a driving force for creep of the neck, which decreases the aforesaid tension. This decrease may be a main reason why the σ_{sa} of Type B in Fig. 4 was considerably smaller than that of Type A in Fig. 5.

4.4. Various stresses generated by the sintering force

The sintering stress, σ_s, must depend on the relative density regardless of pre-firing temperature. Fig. 7, however, shows that σ_{sa} started from a very small value even for a pre-fired specimen with a relatively large ρ, and quickly approached the chain curve. This variation of σ_{sa} suggested a possibility that the present load cell measured not only the sintering force but also other forces generated by shrinkage of the specimen or by an externally applied force. For example, the shrinkage concerned generated elastic deformations in various parts of the self-loading apparatus, especially at contacts such as between the SiC rods and the specimen, between the SiC rods and the

alumina tubs, between Hook I and Timber J, etc. This is because the areas of those contacts were generally so narrow that the effective pressures at them had been considerably multiplied. The force, F_d, causing the aforesaid elastic deformations also caused creep of the specimen, especially at the contacts between the specimen and the SiC rods at (a) and (b) in Fig. 2. If F_d was smaller than the sintering force, F_s, the load cell detected the former force, and the σ_{sa} was the stress, σ_d, defined by Eq. (1) with F_d as F_L.

The Young moduli of alumina [28] and steel [29] are so large that F_d abruptly increased with an increase in shrinkage of the specimen. Furthermore, the contact areas between the specimen and the SiC rods rapidly increased even by a small creep of the specimen, the stress at the contacts concerned rapidly decreased, and hence potential increase in L_1 by the creep quickly decreased. Since shrinkage of a specimen by sintering was considerably fast in the initial and the intermediate sintering stages, the force working to the load cell changed from F_d to F_s during sintering. The σ_{sa} of this stage was the proper sintering stress, σ_s, defined by Eq. (1) with F_s as F_L.

In the case of the specimens both unfired and pre-fired at 1160–1200 °C, σ_{sa} approached the chain curve, and then relatively declined from it. Since the present powder was highly sinterable in commercially available alumina powders, a majority of particles in the green compact of this powder was considered to be homogeneously packed. There must, however, have been a few porous microregions [30–32], in which particles were loosely packed. The sintering stresses in the porous microregions were considerably smaller than the average sintering stress, σ_s. While approaching σ_s, σ_{sa} came to exceed the sintering stresses in the porous microregions [30–32]. The differences between σ_{sa} and the sintering stresses in the porous microregions act as the driving stresses for pore growth in them, reducing the sintering stresses in them. Consequently, the σ_s of the specimen was declining from the proper σ_s of the powder compact in which the pore growth was negligible. The envelope of the σ_{sa} curves in Fig. 7 describes the largest σ_{sa} in those of the curves concerned at a given ρ, approximating the proper relationship between σ_s and ρ. The points of contact between the envelope and the σ_{sa} curves are indicated by the open circles in Fig. 7.

Sintering during pre-firing resulted in not only neck growth but also pore shrinkage, making the specimen tough. When the pre-firing temperature was lower than 1200 °C, the maximum of a σ_{sa} curve increased with an increase in pre-firing temperature. If, however, the pre-firing temperature was higher than 1240 °C, its maximum decreased with increasing pre-firing temperature. These tendencies of the σ_{sa} curves suggested that when the pre-firing temperature was higher than 1200 °C, the aforesaid pore growth had a negligible influence on the variation of σ_{sa}.

The apparent sintering force generated elastic energies in the form of elastic stresses and elastic strains in various parts of the self-loading apparatus, especially at the contacts between them. The value of σ_s abruptly decreased from its maximum at $\rho = 85\%$ to zero at $\rho = 100\%$. There was a critical ρ from which an instantaneous sintering force became smaller than F_L, which was the force, F_{sc}, caused by the energies generated in the various parts of the loading apparatus by a preceding sintering force. The difference between F_{sc} and the instantaneous force acts as the driving force for creep of the specimen, which decreases F_{sc}.

When σ_{sa} was smaller than σ_s, σ_{sa} increased to σ_s during densification, and $d\sigma_{sa}/d\rho$ was positive. In contrast, if σ_{sa} was larger than σ_s, the driving force for the creep increased during densification, accelerating the decrease of F_{sc} or σ_{sa}, and then the negative value of $d\sigma_{sa}/d\rho$ increased. The σ_{sa} satisfying $d\sigma_{sa}/d\rho = 0$, the typical inflection point of a σ_{sa} curve, approximated σ_s, which is showed by a triangle in Fig. 7.

The ρs of the specimens pre-fired to 1320 and 1360 °C were 96.7% and 98.7%, respectively. The shrinkage rates of such dense bodies were very small. The externally applied force also generated the aforesaid elastic energies in various parts of the loading apparatus. The stored energies were spent for creep of the specimen, especially at the contacts between the specimen and the SiC rods. If increase of L_1 by this creep was faster than shrinkage of the specimen by sintering, the load cell measured the force, F_{se}, originating from the externally applied force. The σ_{sa} of this case was the stress σ_{se} defined by Eq. (1) with F_{se} as F_L. The value of σ_{sa} decreased during creep. On the other hand, shrinkage of the specimen increased a load to the load cell, and a reduction of the σ_{sa}, the slope of the σ_{sa} curve, decreased. After σ_s reached σ_{sa}, the predominant stress working to the load cell changed to the stress originating from the preceding sintering force. The difference between σ_{sa} and the instantaneous σ_s, which was the driving force for creep of the specimen, increased during densification, and the decrease of σ_{sa} was accelerated. The slope of the σ_{sa} curve, then, increased from that at the σ_{sa} satisfying $\sigma_{sa} = \sigma_s$. The inflection points of the σ_{sa} curves also approximated σ_ss, which are indicated with the squares in Fig. 7. The dotted curve in this figure is the locus describing the inflection points of the σ_{sa} curves.

Combining the chain and the dotted curves in Fig. 7 shows the convex curve of σ_s, of which the variation range is between 0 and 3.6 MPa. The maximum σ_s was obtained at $\rho = 85\%$. Zuo et al. [24] measured the uniaxial sintering stresses, Σ, of the Al_2O_3 powder of the same series, TM-DAR. The variation of Σ was described by a convex curve, and the largest Σ was obtained at $\rho = 85\%$. Furthermore, the variation of r/r_o was well described by Eq. (3). Although, however, the average radius of the powder was 1.5 times as large as that of the present powder, the maximum of Σ (=3.4 MPa) nearly equaled that of σ_s (=3.6 MPa) in Fig. 7. This indicates that the γ value of the powder used by Zuo et al. was 1.5 times as large as that of the present powder.

4.5. Evaluation of various parameters defining sintering force

Gregg and Rhines [21] derived Eq. (5) relating the surface tension, γ, to the sintering force, F_s.

$$F_s = \gamma \bar{H} A_A a \tag{5}$$

where $\bar{H}$ is an average and local curvature, A_A is the area fraction of porosity cut by a plane, and a is the cross-sectional

area of the specimen perpendicular to the tension caused by the sintering force. The value of $\bar{H}$ was determined by quantitative metallography, using the DeHoff relationship [33]. The γ of copper evaluated from Eq. (5) was 1404–1435 dyne/cm [21], which was close to the directly measured surface tensions of copper, 1430–1670 dyne/cm [34,35]. Rahaman et al. evaluated the sintering stress, Σ, as $\alpha_m \gamma P \bar{H}$, where α_m is a proportionality factor taken to be 1, and P is the porosity [23].

The present powder was so fine that polishing of a partially sintered body resulted in not only exfoliation of some grains from the polishing surface but also round edges between polished grain surfaces and pore surfaces. Large errors were expected for the empirical evaluations of $\bar{H}$, α_m and A_A from the polished surface, and the sintering stresses were estimated based on the geometries of various sintering models with the reported particle sizes [25].

The free-surface-grain-boundary dihedral angle, ψ_s, given by $2\cos^{-1}(\gamma_I/2\gamma)$ is a character determining the local curvature along the pore surface, where γ_I is the grain-boundary tension. Since γ and γ_I respectively vary with the orientations of the surface and the grain boundary, the values of ψ_s are also distributed. Several papers reported the wide distributions of measured dihedral angles, ψ_s, between 76° and 166° for undoped Al_2O_3 [36,37]. The sintering stress σ_s is the sum of distributed sintering forces divided by the product of the relative density and the cross-sectional area of a specimen, being directly related to the average of ψ_s values. In contrast, the distribution mode of ψ_s values must have slightly influence on σ_s. The reported average dihedral angles, ψ_{sm}, were 130.2° [36] and 108° [37]. If ψ_s is smaller than 120°, γ is smaller than γ_I. Slamovich and Lange [30], and Kingery and Francois [31], pointed appreciable pore growth during firing in the case where there were a lot of necks with small ψ_s. Since the present Al_2O_3 powder is highly sinterable, $\psi_{sm} = 130.2°$ was assumed for calculation of the sintering stress. A reported γ value [38] (=0.9 N m^{-1}) was used. A previous paper [39] reported an average coordination number, N_c, equal 6.4 for a green compact with $\rho = 58\%$. The simple cubic packing of particles ($N_c = 6$) is assumed for the calculation of σ_s in the initial sintering stage.

4.6. Sintering stresses evaluated from various sintering models

The stress beneath a pore surface is given by $\gamma(1/r_{p1} + 1/r_{p2})$ [7], where r_{p1} and r_{p2} are respectively the smaller and the larger principal radii of curvature of the pore surface. The sintering force per a particle/grain equals the product of $\gamma(1/r_{p1} + 1/r_{p2})$, the number of pores per a particle/grain, n_p, and the cross-sectional area of a pore, p_s. Since this force equilibrates the product of σ_s and the entire area s_t (the pore surface areas + the grain-boundary areas), σ_s is given by the product $n_p p_s \gamma(1/r_{p1} + 1/r_{p2})/s_t$.

4.6.1. The initial sintering stage

Curve A (large open square symbols) in Fig. 8 shows combining the chain and the broken curves in Fig. 7. Curve B in this figure describes the theoretical σ_s calculated from Eq. (A3)

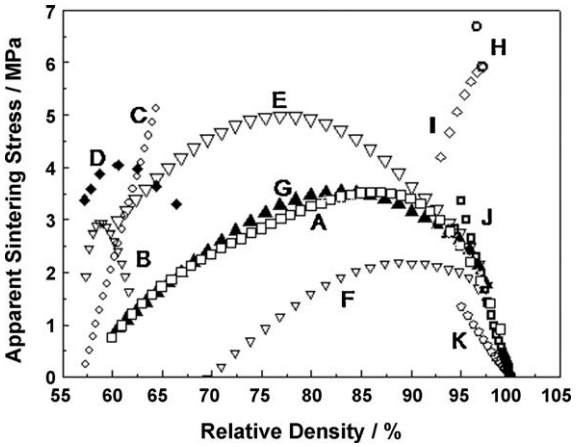

Fig. 8. Sintering stresses evaluated from various sintering models. (A) Combining the broken and the chain curves in Fig. 7: (B) two spheres, (C) a cone normal to a flat surface, (D) polyhedral particles, (E), (F) and (G) intermediate stage sintering of simple cubic packing with straight pores, toroidal pores and modified pores, respectively. (H) and (I) intermediate stage sintering of tetrakaidecahedra with straight pores and toroidal pores, respectively. (J) and (K) final stage sintering of truncated octahedrons with isolated pores, and that of simple cubic packing of grains, respectively.

based on a two-sphere model (Fig. A1(A)) [6–8]. This theoretical σ_s increases abruptly at the beginning of shrinkage and then gradually decreases. The abrupt increase of σ_s occurs by quick neck growth at the beginning of sintering. The gradual decrease of it is attributed to both a decrease of the neck growth rate and the accelerated decrease of β during densification. Curve C in Fig. 8 shows monotonous increase of the theoretical σ_s calculated from Eq. (A3) based on a cone–face contact model (Fig. A1(B)) [40]. This simple increase is a consequence of both monotonous increase of the neck radius and a constant β regardless of a degree of densification.

Simulation on packing of polyhedrons [41] indicated three contacts, point, line and face contacts, of which the percentages were 20%, 60% and 20%, respectively. Face contacts are similar to well-grown necks in the intermediate sintering stage from the geometrical point of view. We assume that sintering of the face contacts skips the initial stage and starts from the intermediate stage. An early-stage sintering model [42] for polyhedral particles suggests combining the initial and the intermediate stages. Eq. (6) is derived to evaluate the sintering stress for polyhedral particles.

$$\sigma_s = C_p\sigma_{sP} + C_l\sigma_{sL} + C_f\sigma_{sF} \quad (6)$$

where σ_{sP}, σ_{sL} and σ_{sF} are respectively the theoretical σ_ss calculated by Eqs. (A3), (A4) and (7). The constants, C_p, C_l and C_f, are the percentages of necks in number for point contacts and for line contacts in the initial stage and that of necks in the intermediate stage, respectively. Curve D in Fig. 8 shows the theoretical σ_s calculated from Eq. (6). All curves B, C and D are markedly higher than the σ_s curve in the range between $\rho = 58\%$ and = 62.5%. Appreciable differences between the theoretical curves and the experimental one suggest that none of the presently examined initial sintering models represent the geometry of necks in a slightly sintered compact.

Initial sintering models suggest no grain growth in common. In contrast, some papers [43,44] pointed particle growth even in very porous compacts, of which SEM micrographs showed a considerable amount of well-grown necks. Particle growth is consistent with the definition for the intermediate sintering stage [9], and sintering data of such particles should be analyzed by equation for intermediate stage sintering.

4.6.2. The intermediate sintering stage

Eqs. (A6) and (A7) were derived respectively based on a simple cubic arrangement of grains with straight pores [39,45] and with toroidal pores [46] in the intermediate sintering stage. The theoretical σ_ss evaluated from Eqs. (A6) and (A7) are shown by curves E and F in Fig. 8, respectively. In a range below $\rho = 95\%$, curve A is between these curves, which suggest that the value of r_{p2} was between the radius of a toroidal pore, $(l - 2r_p)/2$, and ∞, where r_p is the radius of the ideal pore with $\alpha = \pi$. Eq. (7) is derived by replacing $[1 - r_{p1}/r_{p2}]$ in Eq. (A7) with $[1 - 2.1(r_p - 0.07l)/(l - 0.4r_p)]$.

$$\sigma_s = 2\beta\gamma(l - 2r_p)[1 - 2.1(r_p - 0.07l)r_p/(l - 0.4r_p)]/l^2 \quad (7)$$

where $0.07l$ is r_{p1} at $\rho = 97\%$, and 2.1 is the ratio, r_{p1}/r_p. The theoretical σ_s calculated from Eq. (7) is shown by curve G, which is close to curve A in a wide density range between $\rho = 60$–97%.

Eqs. (A9) and (A10) were derived respectively from a tetrakaidecahedra model [9] by the same method as Eqs. (A6) and (A7). Curves H and I in Fig. 8 respectively show the theoretical σ_s values calculated from these equations. Both the curves are quite different from curve A, which indicates that the tetrakaidecahedra model is invalid for the present intermediate sintering stage.

4.6.3. The final sintering stage

Curves J and K in Fig. 8 describe the theoretical σ_ss calculated from Eq. (A14) based on the packing of tetrakaidecahedra [9] and the simple cubic packing of grains [39] in the final sintering stage, respectively. The former curve well describes the experimental data of this sintering stage. Then, the packing of tetrakaidecahedra, which has been generally accepted as the packing of grains in a dense polycrystalline body [47], was valid as a model for the present final sintering stage.

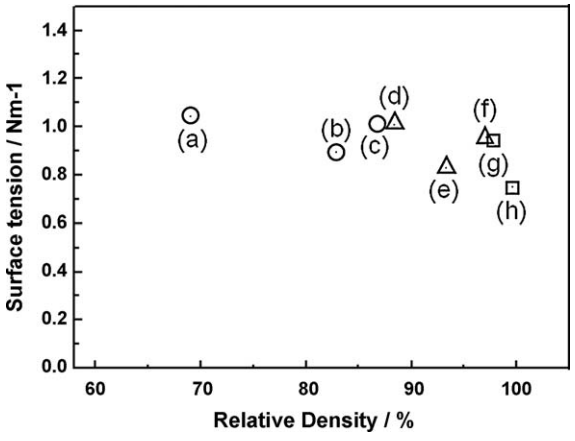

Fig. 9. Surface tensions calculated from Eqs. (6) and (A14) with σ_s marked with circles, triangles and squares in Fig. 7. (a) Unfired, (b) 1160 °C, (c); 1200 °C, (d) 1240 °C, (e) 1260 °C, (f) 1280 °C, (g) 1320 °C and (h) 1360 °C.

4.7. Evaluation of surface tension

The circles, the triangles and the squares in Fig. 9 show the γs calculated from the σ_ss marked with the circles, the triangles and the squares in Fig. 7. They nearly equal a reported surface tension [38].

5. Summary

The sintering stresses of a commercially available alumina powder were measured with a self-loading apparatus. The densification of the part where the axial shrinkage was inhibited was explained by two-dimensional shrinkage. A difference in sintered density between two-dimensional and three-dimensional shrinkages was explained by that between the sums of cross-sectional areas of diffusion paths for those shrinkages. The experimental σ_s data suggest the simple cubic packing of particles for the intermediate sintering stage and the arrangement of tetrakaidecahedra for the final sintering stage. The presently evaluated surface tensions of Al_2O_3 nearly equaled a reported value.

Appendix A

A.1. The initial stage

An angle is expressed by radian. Fig. A1 shows two typical models: (A) two equal spheres with radius r in contact [6–8]

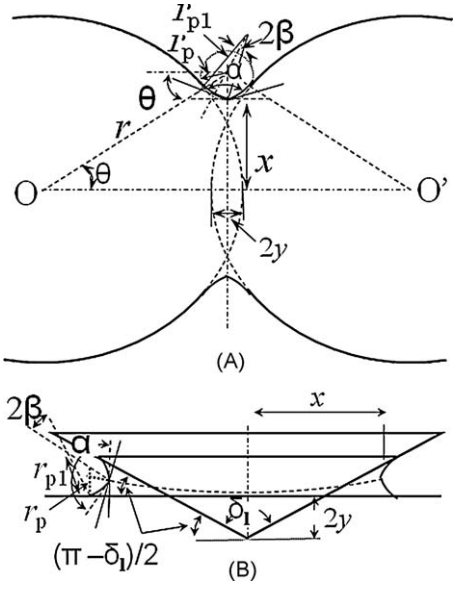

Fig. A1. Two initial sintering models. (A) A schematic neck between two spheres and (B) a cone on a plane.

and (B) cone with apex angle δ_l normal to a flat face [40]. In this figure, α is the grain-boundary groove angle, x is the neck radius, r_{p1} is the minimum radius of curvature of a real neck surface, r_p is the ideal minimum radius of curvature of the neck surface with $\alpha = \pi$, y is a shrinkage between the adjacent centers of particles, and θ is the angle defined by $\cos\theta = (r - r_p)/(r + r_p)$. From models A and B, equations $r_{p1} = r_p \sin(\pi/4 - \theta/2)/\sin\beta$ and $r_{p1} = r_p \sin(\pi + \delta_l)/4/\sin\beta$ are respectively obtained, where the central angle subtending the neck surface, 2β, is $\alpha - \theta - \pi/2$ for model A and $\alpha - 3\pi/4 + \delta_l/4$ for model B. The stress, σ, immediately beneath the neck surface is given by

$$\sigma = \gamma\left[\frac{1}{x} - \frac{1}{r_{p1}}\right] \tag{A1}$$

The force, F_n, generated in the neck surface equals the product of $-\sigma$ and the sectional area of the neck, $4\pi r_p x \sin\beta$ [21], and

$$F_n = 4\pi\gamma \sin\beta\left[\frac{r_p}{r_{p1}}x - r_p\right] \tag{A2}$$

The force per a particle is given by the product of F_n and the coordination number of the particle, N_c. This force equilibrates the product of the average sintering stress, σ_s, and the entire area of the particle (the sum of the pore surface areas and the grain-boundary areas), and hence Eq. (A3) is derived

$$\sigma_s = 4\pi N_c \gamma \sin\beta\left[\frac{r_p}{r_{p1}}x - r_p\right]/k_s r^2 \tag{A3}$$

where k_s is the shape factor related to the entire area of the particle.

A line contact model [42] describes sintering of edge-face contact with four neck surfaces. All the smaller principal curvatures of the neck surfaces are zero. Two neck surfaces in them develop between the faces of adjacent polyhedrons with the contact angle of $\pi - \delta_d$, where δ_d is the dihedral angle of the polyhedrons. The length of these neck surfaces is $4y(1/\tan\theta_1 + 1/\tan\theta_2)$, where θ_1 and θ_2 represent the contact angles of the other neck surfaces perpendicular to these neck surfaces. The sum of θ_1 and θ_2 equals $\pi - \delta_d$, and that of the sectional neck surface areas is $16yr_p \sin\beta_1(1/\tan\theta_1 + 1/\tan\theta_2)$. The central angle subtending the neck surfaces, β_1, is $\alpha/2 - 3\pi/8 + \delta_d/8$.

The length of the rest neck surfaces is given by $\{l/2 + 4y/\tan(\pi - \delta_d)\}$. The sum of the sectional areas of them is $r_p(\sin\beta_2 + \sin\beta_3)\{l/2 + 4y/\tan(\pi - \delta_d)\}$, where β_2 (=$\alpha/2 - \pi/4 + \theta_1/4$) and β_3 (=$\alpha/2 - \pi/4 + \theta_2/4$) are the central angles subtending the rest neck surfaces. The sintering stress based on the line contact model is given by

$$\sigma_s = n_c\gamma\left\{8y\sin\beta_1\left(\frac{1}{\tan\theta_1} + \frac{1}{\tan\theta_2}\right) + (\sin\beta_2 + \sin\beta_3)\left[l + \frac{8y}{\tan(\pi - \delta_l)}\right]\right\}/k_s r^2 \tag{A4}$$

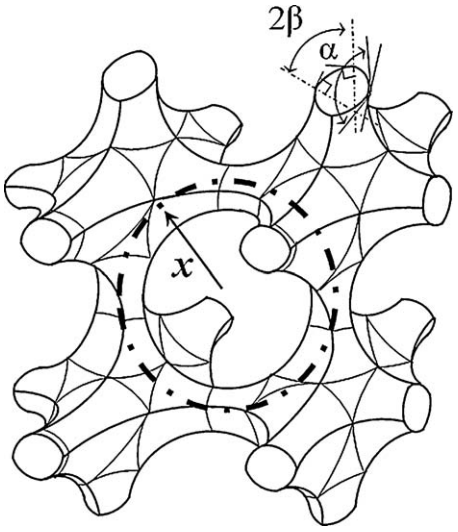

Fig. A2. A schematic model of toroidal porosity in the intermediate stage of sintering.

A.2. The intermediate stage

Fig. A2 shows a schematic model of intermediate sintering, the network of pores in simple cubic packing of grains [39,45]. The porosity of the model is approximated with the two parts, cylindrical porosity along the edges of the particle and cubic porosity at its corners. The porosity, P_o, is given by Eq. (A5).

$$P_o = \left\{3k_{v1}r_{p1}{}^2 l + (8k_{v2} - 6k_{v1})r_{p1}^3\right\}/l^3 \tag{A5}$$

where k_{v1} and k_{v2} are the shape factors related to the volume of pores, and l is the edge length of the cube. The relationship, $r_{p1} = r_p \sin\pi/4 \sin\beta$, is obtained from this figure, where β is $\alpha - \pi/2$. The arc length of a cylindrical pore is $2r_{p1}\sin\beta$. When pores are straight tubes, the principal radii of curvature of the pore surface are r_{p1} and ∞. The stress, σ, immediately beneath the neck surface is given by γ/r_{p1}. The sectional area of a pore is $2r_{p1}(l - 2r_p)\sin\beta$. This polyhedron has 12 edges and 8 corners. The sum of sectional areas of pores is $24r_{p1}\sin\beta(l - 2r_p)$.

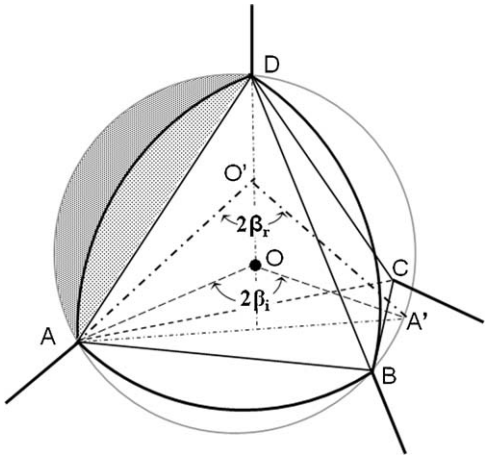

Fig. A3. A schematic pore in the final sintering stage.

The sintering stress, σ_s, is

$$\sigma_s = 4\gamma \sin\beta(l - 2r_p)/l^2 \quad \text{(A6)}$$

Beere reported that toroidal pores formed in the intermediate sintering stage [46]. The larger principal radius of curvature of the pore surface, r_{p2}, is approximated by the radius of the toroids, and Eq. (A6) must be modified as

$$\sigma_s = 4\gamma \sin\beta(l - 2r_p)\left[1 - \frac{r_{p1}}{r_{p2}}\right]/l^2 \quad \text{(A7)}$$

Coble assumed packing of tetrakaidecahedral particles/grains for that of particles/grains in the intermediate and the final sintering stages. According to the intermediate sintering model of Coble, the cross-section of cylindrical pores is a triangle with arched sides, and its sectional area is $2r_{r1}(l - 1.436r_p)\sin\beta$, where $l - 1.436r_p$ is the pore length. A polyhedron has 36 edges and 24 corners. Each edge and each corner are shared by 3 polyhedrons and 4 polyhedrons, respectively. The numbers of cylindrical pores and corners per a polyhedron are 12 and 6, respectively. The porosity is give by

$$P_o = \left\{12k_{v1}{r_p}^2 l + (6k_{v2} - 17.23k_{v1}){r_p}^3\right\}/8\sqrt{2}l^3 \quad \text{(A8)}$$

The whole sectional area of the pores per a polyhedron is $72r_{p1}(l - 1.436r_p)\sin\beta$. The sintering stresses for the tetrakaidecahedra with straight pores and with toroidal pores are respectively

$$\sigma_s = 72\gamma \sin\beta(l - 1.44r_p)/(6 + 12\sqrt{3})l^2 \quad \text{(A9)}$$

$$\sigma_s = 72\gamma \sin\beta(l - 1.44r_p)\left[1 - \frac{r_{p1}}{r_{p2}}\right]/(6 + 12\sqrt{3})l^2 \quad \text{(A10)}$$

A.3. The final sintering stage

Fig. A3 shows a schematic model of a pore in the final sintering stage. Grains are assumed to be tetrakaidecahedra [9,47]. Points A–D are the points at which the edges of the polyhedrons are terminated by the pore surface. Points O and O′ are the centers of the ideal pore surface of $\alpha = \pi$ and a real one of $\alpha < \pi$, respectively. Since a pore surface during this stage is hemispherical, both the principal radii of curvature of the pore surface are equal each other. The angle β_i (=2.46) is the central angle, β, of the ideal pore surface of $\alpha = \pi$. The β for a real pore surface is $\beta_r = 2.46 + \alpha - \pi$. The real principal radius of curvature of a pore surface, r_{p1}, is given by $r_p \sin\beta_i/\sin\beta_r$. If α is π, the porosity is given by $\pi r_p^3/\sqrt{2}l^3$.

The volume and the surface of a hemisphere are respectively calculated from

$$V_h = \pi r_p^3\left[\frac{2}{3} - \cos\beta_q/2 + \frac{1}{3}\cos^3\beta_q/2\right] \quad (q = i \text{ or } r) \quad \text{(A11)}$$

$$S_h = 2\pi r_p^2[1 - \cos\beta_q/2] \quad \text{(A12)}$$

The volume of tetrahedron ABCD in the pore is calculated from

$$V_T = 0.1179 \times \left\{2\sqrt{2/3}r_p\right\}^3$$

The sum of $4 \times V_h$ and V_T approximates the volume of a pore. Eq. (A11) gives $1.086{r_p}^3$ for the V_h value of an ideal pore with $\alpha = \pi$. The aforesaid sum for a spherical pore is apparently larger than its volume ($=4\pi{r_p}^3/3$). This difference is attributed to double counting of the parts on the shaded edges of the polyhedrons in Fig. A3. The volume of shaded parts per a hemisphere is (4.859–4.188)/4.344/4 = 0.0386, which is used for approximation of the volume of a real hemisphere, V_{hr}.

$$V_{hr} = (1 - 0.0386)\pi r_p^3\left[\frac{2}{3} - \cos\beta_r/2 + \frac{1}{3}\cos^3\beta_r/2\right] \quad \text{(A13)}$$

The cross-sectional area of a pore slightly varies with α, and is approximated by $\pi{r_p}^2$. The sintering stress based on the model is given by $(4 \times 6\pi{r_p}^2/r_{p1})\gamma/k_s r^2$, and

$$\sigma_s = 24 \times \pi r_p \gamma\{\sin\beta_r/\sin\beta_i\}/k_s r^2. \quad \text{(A14)}$$

References

[1] E.A. Olevsky, Theory of sintering: from discrete to continuum, Mater. Sci. Eng. R23 (1998) 41.
[2] J. Svoboda, H. Riedel, H. Zipse, Equilibrium pore surfaces, sintering stresses and constitutive equations for the intermediate and late stages of sintering—I. Computation of equilibrium surfaces, Acta Metall. Mater. 42 (1994) 435.
[3] G.N. Hassold, I.W. Chen, D.J. Srolovitz, Computer simulation of final-stage sintering: I, Model, kinetic, and microstructure, J. Am. Ceram. Soc. 73 (1990) 2857.
[4] J. Zhang, P.L. Johnson, Evolution of topology during simulated sintering of powder compacts, J. Am. Ceram. Soc. 76 (1993) 2760.
[5] F. Wakai, Y. Shinoda, T. Akatsu, Methods to calculate sintering stress of porous materials in equilibrium, Acta Mater. 52 (2004) 5621.
[6] G.C. Kuczynski, Self-diffusion in sintering of metallic particles, Trans. AIME 185 (1949) 169.
[7] D.L. Johnson, New method of obtaining volume, grain-boundary, and surface diffusion coefficients from sintering data, J. Appl. Phys. 40 (1969) 192.
[8] M.F. Ashby, A first report on sintering diagrams, Acta Metall. 22 (1974) 275.
[9] R.L. Coble, Sintering crystalline solids. I. Intermediate and final state diffusion models, J. Appl. Phys. 32 (1961) 787.
[10] Y. Oishi, W.D. Kingery, Self-diffusion of oxygen in single crystal and polycrystalline aluminum oxide, J. Chem. Phys. 33 (1960) 480.
[11] K.P.R. Reddy, A.R. Cooper, Oxygen diffusion in magnesium aluminate spinel, J. Am. Ceram. Soc. 64 (1981) 368.
[12] R.J. Brook, Effect of TiO_2 on the initial sintering of Al_2O_3, J. Am. Ceram. Soc. 55 (1972) 114.
[13] C. Greskovich, J.P. Chernoch, Polycrystalline ceramic lasers, J. Appl. Phys. 44 (1973) 4599.
[14] I. Sakaguchi, V. Srikanth, T. Ikegami, H. Haneda, Grain boundary diffusion of oxygen in alumina ceramics, J. Am. Ceram. Soc. 78 (1995) 2557.
[15] B.J. Kellett, F.F. Lange, Thermodynamics of densification: I, Sintering of simple particle arrays, equilibrium configurations, pore stability, and shrinkage, J. Am. Ceram. Soc. 72 (1989) 725.
[16] R.M. Cannon, W.C. Carter, Interplay of sintering microstructures, driving forces, and mass transport mechanisms, J. Am. Ceram. Soc. 72 (1989) 1550.
[17] E.R. Hayward, A.P. Greenough, The surface energy of solid nickel, J. Inst. Met. 88 (1959–1960) 217.

[18] J.J. Gilman, Direct measurements of the surface energies of crystals, J. Appl. Phys. 31 (1960) 2208.
[19] G.C. Benson, G.W. Benson, Surface energies of the alkali halides, Can. J. Chem. 33 (1955) 232.
[20] W. Dawihl, W. Rix, Beeinflussung des Schwundes durch Zugkräfte beim Sintern von Metallpulvern, Z. Metall. 40 (1949) 115.
[21] R.A. Gregg, F.N. Rhines, Surface tension and the sintering force in copper, Metall. Trans. 4 (1973) 1365.
[22] T. Cheng, R. Raj, Measurement of the sintering pressure in ceramic films, J. Am. Ceram. Soc. 71 (1988) 276.
[23] M.N. Rahaman, L.C.De. Jonghe, R.J. Brook, Effect of shear stress on sintering, J. Am. Ceram. Soc. 69 (1986) 53.
[24] R. Zuo, E. Aulbach, J. Rödel, Experimental determination of sintering stresses and sintering viscosities, Acta Mater. 51 (2003) 4563.
[25] T. Ikegami, M. Yokoyama, Y. Moriyoshi, Effects of MgO on the densification of highly sinterable alumina powders, in: The 43rd Symposium on Basic Science of Ceramics, Chiba, Japan, (2004), p. 338.
[26] V.M. Sglavo, P.Z. Cai, D.J. Green, Damage in Al_2O_3 sintering compacts under very low tensile stress, J. Mater. Sci. Lett. 18 (1999) 895.
[27] J.L. Woolfrey, M.J. Bannister, Nonisothermal techniques for studying initial-stage sintering, J. Am. Ceram. Soc. 55 (1972) 390.
[28] E. Ryshkewitch, Oxide Ceramics, Academic Press, New York, 1960, pp. 148–149.
[29] J.D. Lubahn, R.P. Felgar, Plasticity and Creep of Metals, John Wiley & Sons. Inc., New York, 1961, pp. 53–54.
[30] E.B. Slamovich, F.F. Lange, Densification of large pores: II, Driving potentials and kinetics, J. Am. Ceram. Soc. 76 (1993) 1584.
[31] W.D. Kingery, B. Francois, The sintering of crystalline oxides: I, Interactions between grain boundaries and pores, in: G.C. Kuczynski, N.A. Hooton, C.F. Gibbon (Eds.), Sintering Related Phenomena, Gordon and Breach, New York, 1967, pp. 471–496.
[32] A.G. Evans, Structural reliability: a processing-dependent phenomenon, J. Am. Ceram. Soc. 65 (1982) 127.
[33] R.T. DeHoff, F.N. Rhines, Quantitative Microscopy, McGraw Hill, New York, 1969, p. 305.
[34] H. Udin, A.J. Shaler, J. Wulff, The surface tension of solid copper, Trans. AIME 185 (1949) 186.
[35] N.A. Gjostein, F.N. Rhines, Absolute interfacial energies of [001] tilt and twist grain boundaries in copper, Acta Metall. 7 (1959) 319.
[36] T. Ikegami, K. Kotani, K. Eguchi, Some roles of MgO and TiO_2 in densification of a sinterable alumina, J. Am. Ceram. Soc. 70 (1987) 885.
[37] C.A. Handwerker, J.M. Dynys, R.M. Cannon, R.L. Coble, Dihedral angles in magnesia and alumina: distributions from surface thermal grooves, J. Am. Ceram. Soc. 73 (1990) 1371.
[38] W.D. Kingery, G. Economos, M. Humenik, Study of Metal-Ceramic Interactions at Elevated Temperatures, U.S. Atomic Energy Comm., NYO-3144, 1953,, p. 83.
[39] T. Ikegami, Y. Moriyoshi, Intermediate-stage sintering of a homogeneously packed compact, J. Am. Ceram. Soc. 67 (1984) 174.
[40] M.J. Bannister, Shape sensitivity of initial sintering equations, J. Am. Ceram. Soc. 51 (1968) 548.
[41] T. Ikegami, Contacts and coordination numbers in a compact of polyhedral particles, J. Am. Ceram. Soc. 79 (1996) 148.
[42] T. Ikegami, Early-stage sintering in a powder compact of polyhedral particles I. Models, Ceram. Int. 25 (1999) 415.
[43] C. Greskovich, K.W. Lay, Grain growth in very porous Al_2O_3 compacts, J. Am. Cream. Soc. 55 (1972) 142.
[44] Y. Moriyoshi, W. Komatsu, Kinetics of initial sintering with grain growth, J. Am. Cream. Soc. 53 (1970) 671.
[45] A.K. Kakar, Sintering kinetics based on geometric models, J. Am. Ceram. Soc. 51 (1968) 236.
[46] W. Beere, A unifying theory of the stability of penetrating liquid phases and sintering pores, Acta Metall. 23 (1975) 131.
[47] B. Chalmers, Physical Metallurgy, John Wiley & Sons Inc., New York, 1959, pp. 113–122.